MATERIALS SCIENCE

Exceptional oxygen evolution reactivities on $CaCoO_3$ and $SrCoO_3$

Xiang Li[1,2]*, Hao Wang[1]*, Zhiming Cui[1], Yutao Li[1†], Sen Xin[1], Jianshi Zhou[1], Youwen Long[3,4], Changqing Jin[3], John B. Goodenough[1†]

We investigated the roles of covalent bonding, separation of surface oxygen, and electrolyte pH on the oxygen evolution reaction (OER) on transition metal oxides by comparing catalytic onset potentials and activities of $CaCoO_3$ and $SrCoO_3$. Both cubic, metallic perovskites have similar Co^{IV} intermediate spin states and onset potentials, but a substantially smaller lattice parameter and shorter surface oxygen separation make $CaCoO_3$ a more stable catalyst with increased OER activity. The onset potentials are similar, occurring where H^+ is removed from surface -OH^-, but two competing surface reactions determine the catalytic activity. In one, the surface -O^- is attacked by electrolyte OH^- to form the surface -OOH^-; in the other, two -O^- form a surface peroxide ion and an oxygen vacancy with electrolyte OH^- attacking the oxygen vacancy. The second pathway can be faster if the surface oxygen separation is smaller.

INTRODUCTION

The air electrodes of electrochemical water-splitting systems and metal-air rechargeable batteries require a high catalytic activity at room temperature of the oxygen evolution reaction (OER) and long-term structural stability of the catalyst in an alkaline medium (*1*–*5*). Traditional OER catalysts of acceptable catalytic activity at room temperature such as carbon-supported noble metals and RuO_2 or IrO_2 are too expensive and/or unstable under anodic (charging) conditions (*6*–*8*). Low-cost transition-metal oxides have been demonstrated to be promising OER catalysts (*9*–*15*). AMO_3 perovskites are attractive for the study of the OER because their electrochemical potential and electronic properties can be systematically controlled by cation substitutions on both the A and M sites with different valences and ionic sizes (*16*–*18*), but the relative merits of π* antibonding versus σ* antibonding orbitals of d-electron symmetry, the degree of metal d and oxygen 2p orbital mixing at the active sites, the separation of the surface oxygens, and the pH dependence of the catalytic activity have been little explored.

Here, we report a comparative study of the catalytic activities of two isostructural $ACoO_3$ (A = Ca, Sr) perovskites that have been synthesized under high pressure and characterized physically (*19*, *20*). Each perovskite is cubic and metallic; they exhibit long-range magnetic order, indicating a $t^4\sigma^{*1}$ intermediate spin state on a Co^{IV} formal valence state. The π* antibonding t^4 electrons are localized in $SrCoO_3$; they are at the crossover from localized to itinerant behavior in $CaCoO_3$, which has a notably shorter Co—O bond length than that of $SrCoO_3$ (1.87 Å versus 1.92 Å). The itinerant character of the σ* electrons is responsible for the metallic conductivity and the lack of a cooperative Jahn-Teller distortion of the $CoO_{6/2}$ sites that would be expected with localized e^1 electrons.

The oxygen emitted by the OER comes from the alkaline medium either directly or indirectly via an extraction of oxygen from the catalyst that is replaced from the medium. Which route is taken depends on the separation of the surface oxygen, the zeta point of the catalyst, and the pH of the alkaline medium; at the zeta point; the adsorbed water or OH^- on oxide particles immersed in an aqueous medium does not change the pH of the medium (*1*). Acidic oxides immersed in pH 7 water make the water acidic by losing surface H^+ to medium H_2O forming H_3O^+ ions; basic oxides attract H^+ from a pH 7 medium, -O^{2-} + H_2O = -OH^- + OH^-, to render the medium alkaline. In a strongly alkaline medium, the $ACoO_3$ perovskites are acidic, i.e., they lose surface H^+ to the medium: -$CoOH^-$ + OH^- = -CoO^{2-} + H_2O. In oxidation in an anodic current, -CoO^{2-}-e^- = -CoO^-, the O^- ion is vulnerable to attack by a medium OH^- to form -$CoOOH^-$ or, alternatively, to the reaction -2CoO^- = -$Co(O_2)^{2-}$ + Co-□ followed by occupancy of the surface oxygen vacancy □ either by medium OH^- or by a lattice oxygen. The creation of the surface CoO^- species may determine the onset potential, but the subsequent OER activity may depend on which subsequent route is faster and, therefore, on the separation of the surface oxygen. These competing interactions would give rise to different ratios of the catalyst and medium oxygen in the evolved O_2. By using the ^{18}O isotope in the catalyst, Grimaud *et al.* (*21*) have found zero, one, or two ^{18}O in the evolved O_2, which indicates that the two routes are both operative and that the separation of the surface oxygen may determine the activity of the OER following the onset potential.

RESULTS

Crystal structure of $ACoO_3$ (A = Ca, Sr)

The Rietveld refined powder X-ray diffraction (XRD) patterns of high-pressure $ACoO_3$ (A = Ca, Sr) and their structural information are shown in Fig. 1 and table S1. Both $CaCoO_3$ and $SrCoO_3$ have a cubic perovskite structure (space group: *Pm*-3*m*) with corner-shared $CoO_{6/2}$ octahedra and Ca^{2+} or Sr^{2+} on the 12-fold coordinated A sites. $CaCoO_3$ has the smaller lattice parameter (table S1) because of the smaller ionic radius of Ca^{2+} than Sr^{2+} ions, and the nearest Co—O bond length is decreased by $\Delta r \approx 0.05$ Å from $SrCoO_3$ to $CaCoO_3$. The particle sizes of the $ACoO_3$ (A = Ca, Sr) were about 10 μm (fig. S1), and energy-dispersive X-ray spectroscopy mapping in fig. S2 revealed a uniform distribution of Ca, Sr, Co, and O elements in the particles. A high-resolution transmission electron microscopy (TEM) image of $ACoO_3$ in Fig. 1 (B and C) confirmed a homogeneous

[1]Materials Science and Engineering Program and Texas Materials Institute, The University of Texas at Austin, Austin, TX 78712, USA. [2]Key Laboratory of Advanced Optoelectronic Quantum Architecture and Measurement, Ministry of Education (MOE), School of Physics, Beijing Institute of Technology, Beijing 100081, China. [3]Beijing National Laboratory for Condensed Matter Physics and Institute of Physics, Chinese Academy of Sciences, Beijing 100190, China. [4]Songshan Lake Materials Laboratory, Dongguan 523808, Guangdong, China.
*These authors contributed equally to this work.
†Corresponding author. Email: lytthu@utexas.edu (Y.Li.); jgoodenough@mail.utexas.edu (J.B.G.)

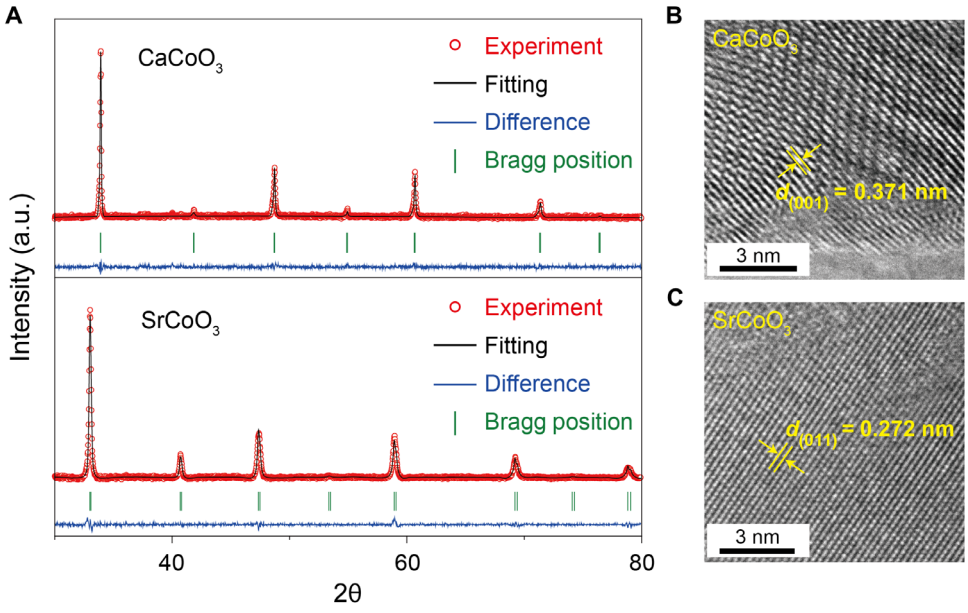

Fig. 1. The structure of $ACoO_3$(A = Ca, Sr). (**A**) Observed, calculated, and difference patterns for the Rietveld refinement from the XRD of cubic $ACoO_3$. a.u., arbitrary units. (**B** and **C**) TEM images of $ACoO_3$ (A = Ca, Sr).

and well-crystallized structure of the surface and bulk of $ACoO_3$ (A = Ca, Sr). The oxygen stoichiometry of each $ACoO_3$ (A = Ca, Sr) was studied with cyclic voltammetry (CV); Co_3O_4 and $LaCoO_3$ with no oxygen vacancies were tested for comparison (fig. S3). The reversible reduction/oxidation peaks at 1.0 to 1.2 V versus a reversible hydrogen electrode (RHE) in the CV of $SrCoO_3$ correspond to the insertion (oxidation) reaction, $SrCoO_{3-x} + 2xOH^- \rightarrow SrCoO_3 + xH_2O + 2xe^-$, indicating that some oxygen vacancies existed; the absence of these peaks in $CaCoO_3$, Co_3O_4, and $LaCoO_3$ confirmed their stoichiometric composition.

OER performance of (A = Ca, Sr)

The OER performances of $ACoO_3$ (A = Ca, Sr, La), commercial Co_3O_4, and RuO_2 are shown in Fig. 2 (A to D) and table S2; the current density of all samples in the linear sweep voltammograms was normalized to the electrochemically active surface area to exclude geometric effects (fig. S4 and table S2). $CaCoO_3$ has the highest OER activity with an onset potential of 1.48 V versus RHE and a small overpotential of 0.26 V at 10 mA cm^{-2}. $SrCoO_3$ shows almost the same onset potential (1.51 V) as that of RuO_2 (1.50 V). The smaller Tafel slopes of $CaCoO_3$ and $SrCoO_3$ in Fig. 2C compared to those of RuO_2, $LaCoO_3$ with intermediate-spin t^5e^1 at 25°C of the surface Co(III), and Co_3O_4 indicate their superior OER kinetics. The perovskite $LaCoO_3$ and spinel Co_3O_4 with larger surface O—O separation at 25°C exhibit a negligible catalytic activity compared with those of $ACoO_3$ (A = Ca, Sr).

The electronic structure of (A = Ca, Sr)

The Co—O bond lengths of the perovskites $CaCoO_3$, $SrCoO_3$, and $LaCoO_3$ are 1.867, 1.915, and 1.930 Å, respectively. The 180° Co—O—Co interaction in cubic $ACoO_3$ (A = Ca, Sr) is strong enough to form a half-filled antibonding σ* itinerant-electron up-spin band (Fig. 3). The temperature dependence of resistivity in Fig. 3A of $ACoO_3$ (A = Ca, Sr) shows a metallic behavior down to 2 K, and the electronic conductivity of $CaCoO_3$ is one order of magnitude higher than that of $SrCoO_3$. The higher electronic conductivity of $CaCoO_3$ than $SrCoO_3$ reduces the charge transfer resistance (R_{ct}) and the ohmic potential drop of $CaCoO_3$ during the OER (fig. S5A), and the R_{ct} values of $CaCoO_3$ and $SrCoO_3$ are one order of magnitude smaller than those of the electronic insulators $LaCoO_3$ and Co_3O_4 at potentials above 1.4 V (figs. S5A and S6). The magnetic properties of $CaCoO_3$ and $SrCoO_3$ were investigated to study the electron configuration of Co^{IV} ions (Fig. 3A), which affects their interaction with the reaction intermediates and their OER activity. An effective magnetic moment $\mu_{eff} = 4.1\ \mu_B$ was obtained for $CaCoO_3$ by fitting with the Curie-Weiss law, indicating that the Co^{IV} ions of $CaCoO_3$ have the intermediate spin state ($t_2^4\sigma^{*1}$) with $S = 3/2$ (Fig. 3B). $SrCoO_3$, which also adopts the intermediate-spin electron configuration, has a ferromagnetic transition at 300 K in the magnetization. For comparison, the spin state of Co^{III} ions in $LaCoO_3$ (Co^{3+}: d^6) can be described by a d^6 mixed-spin scenario in which the ratio of the low-spin (LS) ground state (t^6e^0, $S = 0$) and the high-spin (HS) excited state (t^4e^2, $S = 2$) is roughly unity at room temperature (fig. S7) (*22*), while the Co^{III} ions in spinel Co_3O_4 are in the LS state (t^6e^0, $S = 0$) (Fig. 3B). Moreover, the π* and σ* bandwidths are greater in $CaCoO_3$ with the shorter Co^{IV}—O^{2-} bond than in $SrCoO_3$ (Fig. 3C).

Figure 4 and fig. S8 compare the onset potentials and the OER activity of $CaCoO_3$ versus $SrCoO_3$, Co_3O_4, $LaCoO_3$, and RuO_2 in O_2-saturated KOH, with pH varying from 12.5 to 14. The onset potentials of the two perovskites are similar, but the activity of the OER is much higher on $CaCoO_3$ than on $SrCoO_3$. The activities of the two Co^{IV} perovskites are substantially higher than those of the two Co^{III} oxides. In each case, the catalytic activity and onset potential show a dependence on the pH of the KOH solution.

The stability of $ACoO_3$ (A = Ca, Sr)

The durability of all samples tested at 1.6 V in an O_2-saturated 0.1 M KOH solution is shown in Fig. 2D and fig. S5B. $CaCoO_3$ had the best durability. It retained more than 90% of its initial current density after

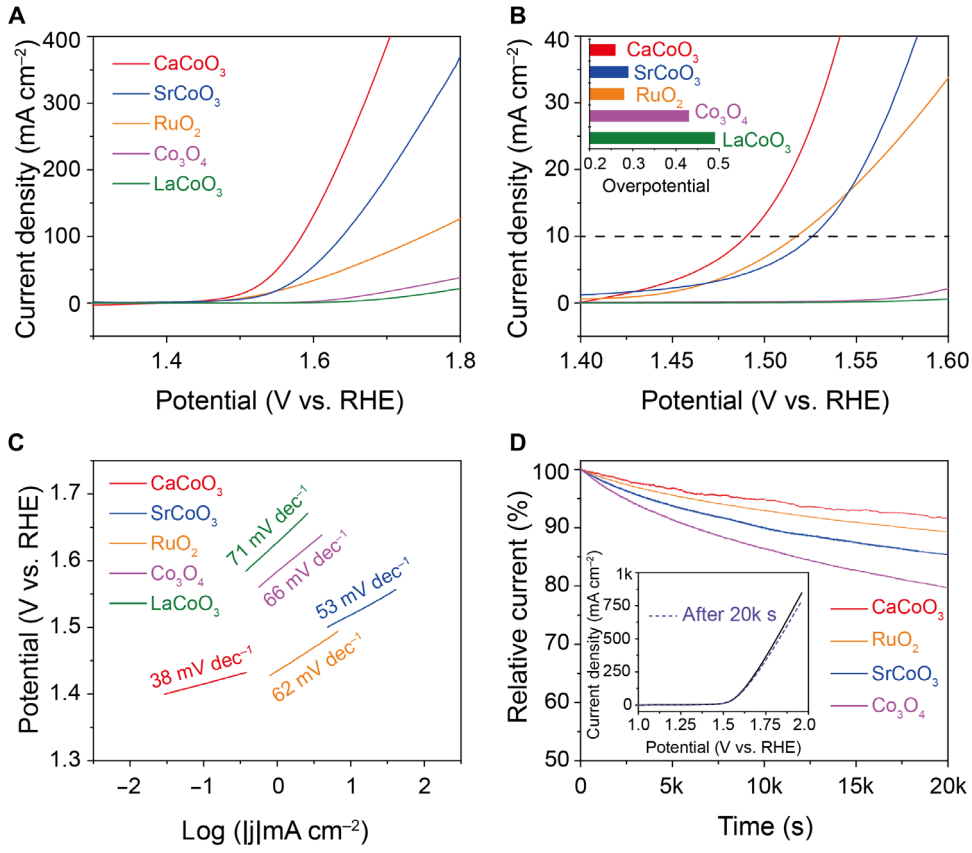

Fig. 2. OER performance of $ACoO_3$(A = Ca, Sr), RuO_2, $LaCoO_3$, and Co_3O_4. (**A**) Linear sweep voltammograms at 1600 rpm in 0.1 M KOH. (**B**) Overpotential required at 10 mA cm^{-2}. (**C**) Tafel slopes. (**D**) Chronoamperometric curves in an O_2-saturated 0.1 M KOH electrolyte at 1.6 V versus RHE.

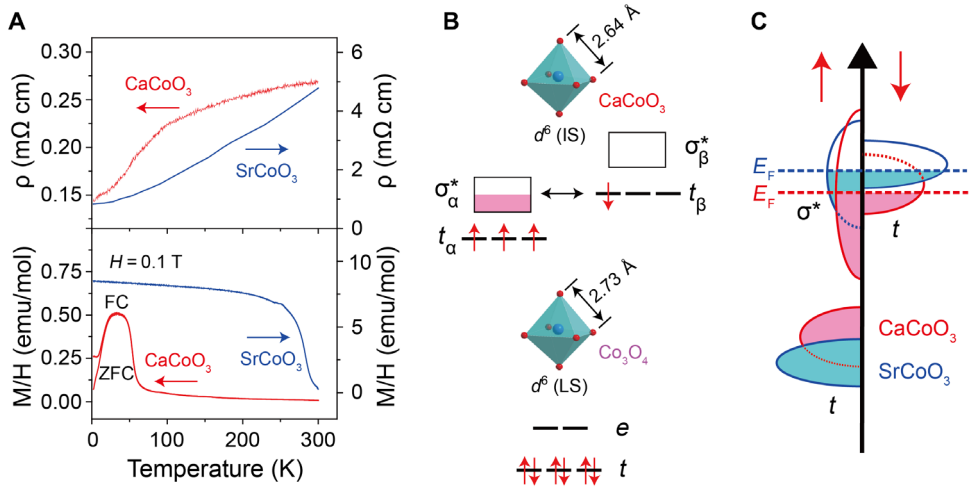

Fig. 3. Magnetic and transport properties of $ACoO_3$(A = Ca, Sr). (**A**) Temperature dependence of resistivity measured at zero field [$CaCoO_3$ (red curve), $SrCoO_3$ (blue curve digitized from (*20*)] temperature dependence of magnetization in both zero-field cooling (ZFC) and field cooling (FC). (**B**) Electronic spin states of the octahedral site Co ions of $ACoO_3$ (A = Ca, Sr) and Co_3O_4. (**C**) Schematic band diagrams of $ACoO_3$ (A = Ca, Sr). IS, intermediate spin.

20,000 s and still kept about 89% of its initial current density after 50,000 s. The same OER activity of $CaCoO_3$ after the measurement as the fresh sample (Fig. 2D, inset) indicates a good stability of $CaCoO_3$ in alkaline solution. The XRD (Fig. 5A) and Raman results (Fig. 5B) of $ACoO_3$ (A = Ca, Sr) after the OER testing show that the samples retain the same cubic perovskite structure, and the TEM image of $ACoO_3$ (A = Ca, Sr) before and after OER testing confirms that the surfaces of the particles retain a crystalline structure (Fig. 5, C and D). The strong

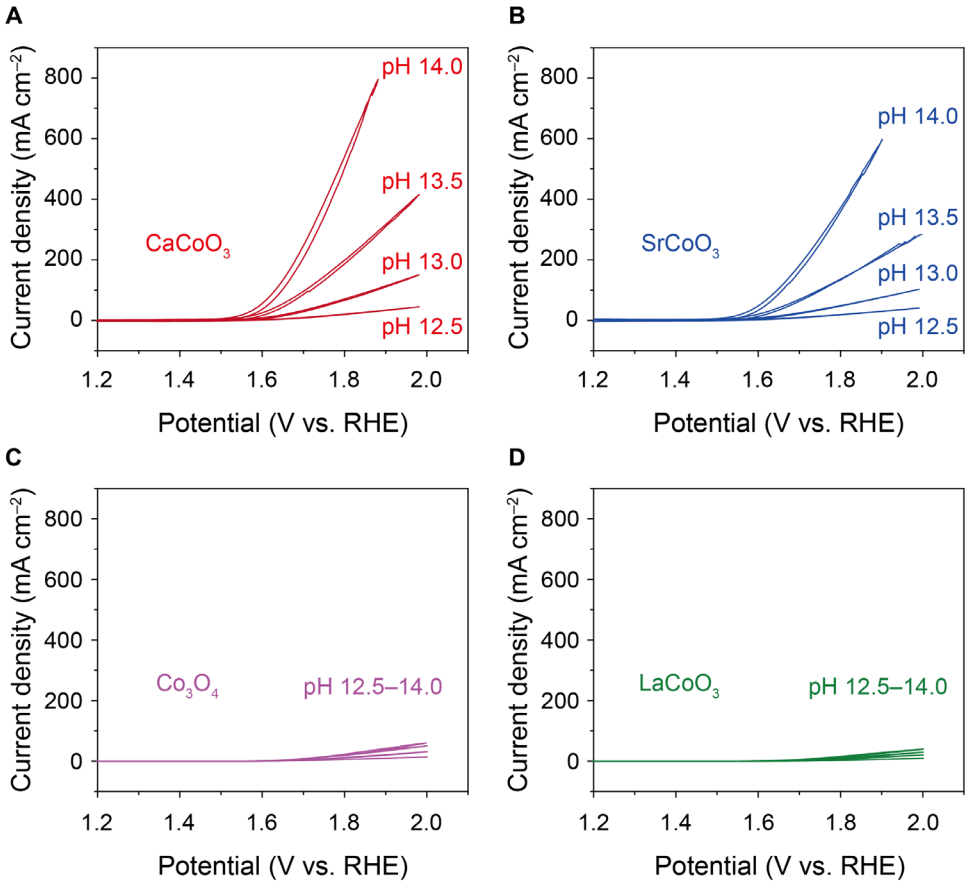

Fig. 4. OER performance of $ACoO_3$(A = Ca, Sr) in alkaline solutions with different pH. (**A** to **D**) CV measurements in O_2-saturated KOH with pH 12.5 to 14, showing the pH-dependent OER activity of $ACoO_3$ (A = Ca, Sr) on the RHE scale.

Co—O bond of $CaCoO_3$ increases its stability in alkaline solution. The oxygen deficiency in $SrCoO_3$ is the result of a weaker Co—O bond.

DISCUSSION

The energy of the Co^V state is below the top of the O-2p bands. Therefore, the removal of an electron from an $ACoO_3$ perovskite surface during charge cannot oxidize Co^{IV} to Co^V; electrons are removed from surface oxygen. In KOH solution at low pH, the electron removal reaction is

$$-Co(OH)^- + OH^- - e^- = -CoO^- + H_2O \quad (1)$$

because the strong attraction of the Co for the O-2p electron weakens the attraction of surface oxygen for the surface proton relative to the attraction of the medium OH^-. The charging voltage needed to create a surface $-CoO^-$ species is the onset potential of the OER. At high pH, the surface proton is removed chemically to form $-CoO^{2-}$ in the reaction

$$-CoOH^- + OH^- = -CoO^{2-} + H_2O \quad (2)$$

and electron removal during charge at the onset potential is

$$-CoO^{2-} - e^- = -CoO^- \quad (3)$$

The surface $-CoO^-$ may be attacked by a solution OH^- in the reaction

$$-CoO^- + OH^- - e^- = -CoOOH^- \quad (4A)$$

that is followed by

$$-CoOOH^- + OH^- = -Co(O_2)^{2-} + H_2O \quad (4B)$$

The activity of the OER after its onset depends on the rates of the reactions (4) and an alternative mechanism for the formation of the peroxide ion $(O_2)^{2-}$ by a direct O^-—O^- interaction, which would be faster if the surface O—O separation is shorter

$$-2CoO^- + OH^- = -Co(O_2)^{2-} + -Co(OH)^- \quad (5)$$

Reaction 5 may compete with reaction 4. Reaction 1 is the step that determines the onset potential. The shorter Co—O bond length of $CaCoO_3$ relative to that of $SrCoO_3$ may not only lower the onset potential of reaction 1 but also increase the activity by reducing the surface oxygen separation to increase the rate of reaction 5 relative to that of reaction 4. Once the peroxide ion $(O_2)^{2-}$ is formed,

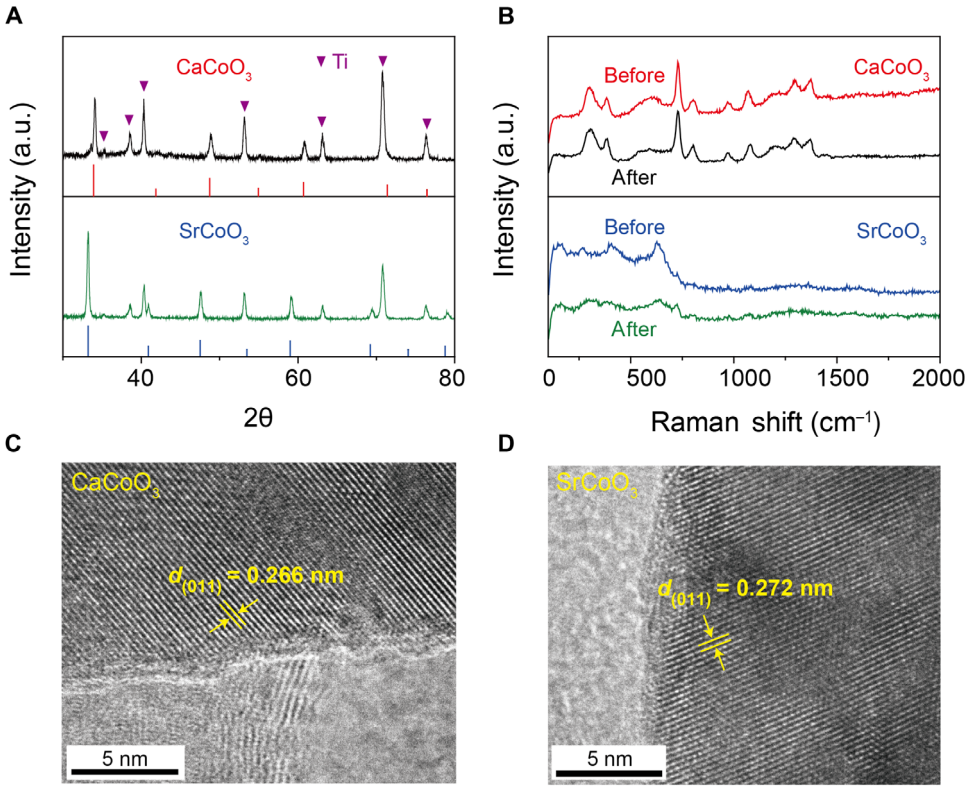

Fig. 5. The durability of $ACoO_3$(A = Ca, Sr). (**A** to **D**) XRD, Raman spectra, and TEM results of $ACoO_3$ (A = Ca, Sr) after OER testing.

the reaction $-Co(O_2)^{2-} - 2e^- + OH^- = -Co(OH)^- + O_2\uparrow$ should not be rate limiting.

The Co^{III} ions in Co_3O_4 and $LaCoO_3$ can be oxidized to Co^{IV}, but the onset potential for reaction 1 is necessarily higher starting from Co^{III} rather than Co^{IV}. Figure S3 confirms that a greater removal of electrons before deprotonation occurs in Co_3O_4 than in $ACoO_3$, with A = Ca or Sr.

Increasing the concentration of Co^{IV} in the chemically/electrochemically delithiated $Li_{1-x}CoO_2$ has been reported to increase the OER activity. A metallic layer on the $Li_{1-x}CoO_2$ phase with LS Co^{IV}/Co^{III} ions was obtained at $x = 0.5$, and at $x > 0.5$, the peroxide $(O_2)^{2-}$ forms on the surface of $Li_{1-x}CoO_2$; as x increases, oxygen gas is released. As the formal valence of the cobalt increases, its Fermi level approaches and crosses the top of the O-2p bands in the layered $Li_{1-x}CoO_2$, which lowers the energy of back electron transfer from the oxygen to the cobalt and increases the O-2p character in the hybrid orbitals of Co-d symmetry. On oxidation, removal of electrons creates surface electron holes in the hybrid orbitals and, therefore, increasingly on the oxygen as the formal Co valence is increased. The top of the O-2p bands in the $ACoO_3$ perovskites is lower with respect to the hybrid antibonding orbitals of d-wave symmetry than in the layered $Li_{1-x}CoO_2$, which is why the Co^{IV} valence is stable in the $ACoO_3$ perovskites, but the shorter the Co—O bond, the larger the O-2p and Co-3d overlap integrals and their hybridization.

Oxygen species (water or OH^-) are adsorbed on the perovskite to complete the sixfold coordination of the cobalt, and the surface protons reach equilibrium with the medium pH. The proton transfer from the catalyst to the medium can be either a single chemical transfer reaction 2 or a proton-electron transfer step as shown in reactions 1 and 4 above. Two possible OER mechanisms are shown in Fig. 6; electron transfer from the electrocatalyst at an applied onset potential creates an O^- intermediate with an electron hole that can be attacked by the medium OH^- to form OOH (step 2 in Fig. 6D) or two neighboring O^- may react as in reaction 5. The former involves a second removal of H^+, whereas the latter does not, which may make the latter the faster mechanism.

CONCLUSIONS

The $ACoO_3$ (A = Ca or Sr) cubic perovskites synthesized under high pressure have been studied as OER electrocatalysts in KOH solution. The high-pressure synthesis stabilizes the Co^{IV} ion in an intermediate spin-state configuration $t^4\sigma^{*1}$ in which the σ* antibonding orbitals of d-wave symmetry are itinerant, whereas the π* antibonding orbitals of d-wave symmetry are localized in $SrCoO_3$ and are at the crossover to itinerant behavior in $CaCoO_3$. Both perovskites are cubic, but $CaCoO_3$ has a much shorter Co—O bond length and larger σ* bandwidth indicative of a greater O-2p character in the states of d-wave symmetry. The smaller onset potentials with Co^{IV} than Co^{III} oxides show the importance of admixing O-2p orbitals in the states of d-wave symmetry for the OER. Nevertheless, the larger σ* bandwidth of $CaCoO_3$ versus $SrCoO_3$ has little influence on the onset potential of the OER, but it does stabilize the catalyst. The rate-limiting step responsible for the OER is the formation of surface peroxide ions $(O_2)^{2-}$. The substantially greater OER activity on $CaCoO_3$ than $SrCoO_3$ indicates a larger component of a faster mechanism than on $SrCoO_3$, which suggests that the shorter

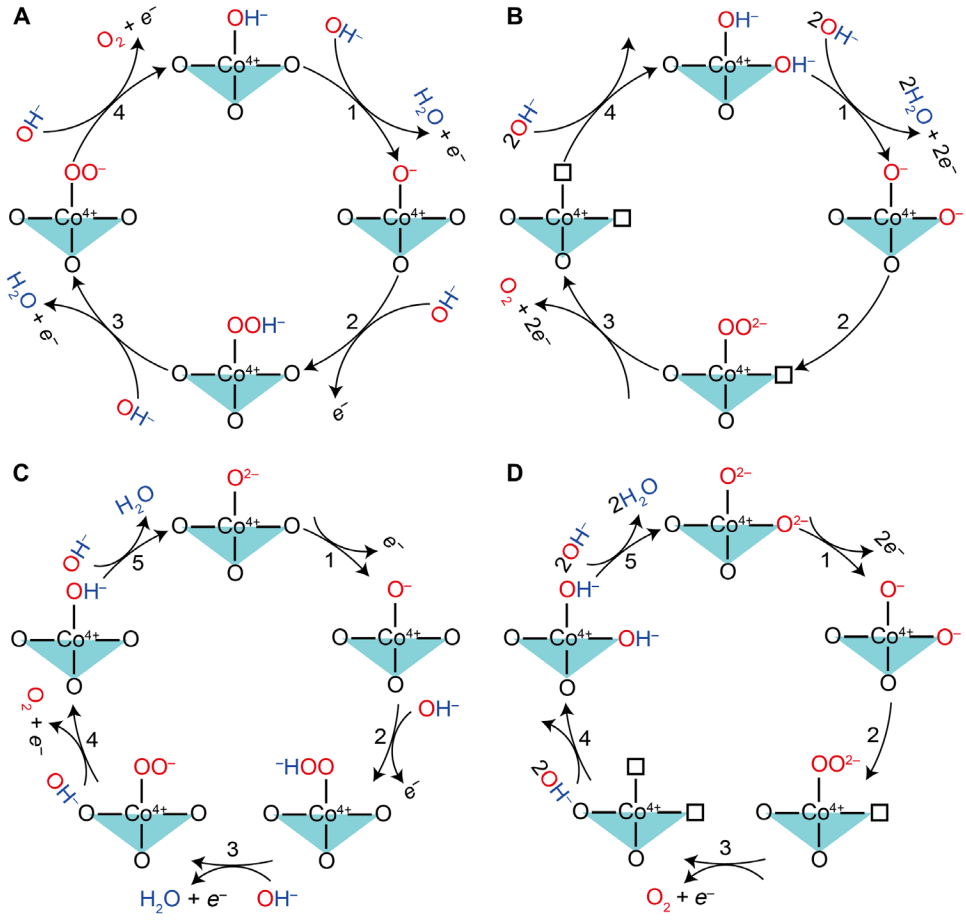

Fig. 6. Possible OER mechanisms in $ACoO_3$(A = Ca, Sr). (**A**) Conventional OER mechanism involving four proton-electron transfer steps on the active surface metal sites. (**B**) OER mechanism with surface lattice oxygen activated for OER to form peroxide and evolve O_2. (**C** and **D**) Two proposed OER mechanisms based on the Co^{4+}—O^{2-} bond; the deprotonation process by OH^- is finished by a chemical step (step 5) rather than a proton/electron-coupled transfer step.

separation of surface oxygen in $CaCoO_3$ may be favoring reaction 5 relative to reaction 4. This suggestion warrants further experimental verification.

MATERIALS AND METHODS

The precursors of oxygen-deficient perovskites $CaCoO_{3-\delta}$ and $SrCoO_{3-\delta}$ were prepared by solid-state reaction. The mixture of $CaCO_3$ (or $SrCO_3$) (Alfa Aesar, 99.99%) and Co_3O_4 (Alfa Aesar, 99.99%) with a stoichiometric ratio was thoroughly ground and sintered at 1000°C for 48 hours. High-pressure syntheses of the cubic $CaCoO_3$ and $SrCoO_3$ perovskites were performed under 7 GPa and at 1200°C with a Walker-type multianvil module (Rockland Research Co.). The precursors were pressed into pellets and sealed in a platinum crucible with the oxygen-releasing agent $KClO_4$. Each crucible was contained in a Mo heater surrounded by a $LaCrO_3$ sleeve for thermal insulation. Cr-doped MgO octahedra with pyrophyllite gaskets were used as the pressure medium. The phase purity of the obtained products was examined by powder XRD at room temperature with a Philips X'Pert diffractometer (Cu K_α radiation). Structural parameters were obtained by refining the XRD patterns with the software FULLPROF. DC magnetic susceptibility was measured with a commercial Superconducting Quantum Interference Device (SQUID) magnetometer (Quantum Design). Resistivity data were collected using the Physical Property Measurement System (PPMS; Quantum Design).

The morphology and microstructures of the samples were investigated using field-emission scanning electron microscope (Quanta 650) and TEM. Raman spectroscopy was carried out with a WITec alpha 300 Raman microscope instrument (WITec, Germany) equipped with a 532-nm wavelength laser for excitation.

All electrochemical measurements were carried out using an Autolab electrochemical workstation with a conventional three-electrode system in O_2-saturated KOH solution. The Hg/HgO electrode, Pt, and glassy carbon electrode (GCE; 5 mm in diameter) were used as the reference, counter, and working electrodes, respectively. All the potential values were calibrated to the RHE. The catalyst inks were prepared as follows: 5 mg of the catalyst and 20 μl of 5 weight % Nafion were dispersed in 1000 μl of isopropanol. Ten microliters of the catalyst ink with a catalyst loading of 0.25 mg cm^{-2} was dropped onto the GCE and dried at room temperature. The OER characterizations were carried out using a glassy carbon rotating disc electrode at a rate of 1600 rpm. The CV and linear sweep voltammetry measurements were performed at a rate of 50 and 5 mV s^{-1}, respectively. The chronoamperometric responses were conducted on a fixed potential of 1.55 V in O_2-saturated 0.1 M KOH solution. The electrochemical impedance spectroscopy (EIS) was measured using an Autolab workstation with

an applied frequency range from 10^6 to 0.1 Hz. Titanium foil was used as the substrate while testing the materials after cycling.

SUPPLEMENTARY MATERIALS

Supplementary material for this article is available at http://advances.sciencemag.org/cgi/content/full/5/8/eaav6262/DC1

Fig. S1. SEM images and particle size distribution of $CaCoO_3$ and $SrCoO_3$.
Fig. S2. Elemental distribution of $CaCoO_3$ and $SrCoO_3$.
Fig. S3. CV curves of Co-based catalysts.
Fig. S4. Double-layer capacitance measurement to determine the electrochemically active surface area of $CaCoO_3$ and RuO_2.
Fig. S5. The impedance plots and cycling stability of the catalysts studied in this work.
Fig. S6. Response of charge transfer resistance (R_{ct}) to applied potential of the catalysts studied in this work to applied potential in the solution of pH 12.5, 13, 13.5, and 14.
Fig. S7. The intermediate spin state of Co^{III} in LaCoO3 (t^4e^1, $S = 1$) at 25°C.
Fig. S8. pH-dependent OER activity of RuO_2 in O_2-saturated KOH with pH 12.5 to 14.
Table S1. Structural refinements of $CaCoO_3$ and $SrCoO_3$ obtained at room temperature.
Table S2. OER activity and ECSA of all studied catalysts.

REFERENCES AND NOTES

1. J. B. Goodenough, R. Manoharan, M. Paranthaman, Surface protonation and electrochemical activity of oxides in aqueous solution. *J. Am. Chem. Soc.* **112**, 2076–2082 (1990).
2. D. A. Kuznetsov, B. Han, Y. Yu, R. R. Rao, J. Hwang, Y. Román-Leshkov, Y. Shao-Horn, Tuning redox transitions via inductive effect in metal oxides and complexes, and implications in oxygen electrocatalysis. *Joule* **2**, 225–244 (2018).
3. J. Hwang, R. R. Rao, L. Giordano, Y. Katayama, Y. Yu, Y. Shao-Horn, Perovskites in catalysis and electrocatalysis. *Science* **358**, 751–756 (2017).
4. W. T. Hong, K. A. Stoerzinger, Y.-L. Lee, L. Giordano, A. Grimaud, A. M. Johnson, J. Hwang, E. J. Crumlin, W. Yang, Y. Shao-Horn, Charge-transfer-energy-dependent oxygen evolution reaction mechanisms for perovskite oxides. *Energ. Environ. Sci.* **10**, 2190–2200 (2017).
5. Z. Cui, Y. Li, G. Fu, X. Li, J. B. Goodenough, Robust Fe_3Mo_3C supported IrMn clusters as highly efficient bifunctional air electrode for metal–air battery. *Adv. Mater.* **29**, 1702385 (2017).
6. J. T. Mefford, X. Rong, A. M. Abakumov, W. G. Hardin, S. Dai, A. M. Kolpak, K. P. Johnston, K. J. Stevenson, Water electrolysis on $La_{1-x}Sr_xCoO_{3-\delta}$ perovskite electrocatalysts. *Nat. Commun.* **7**, 11053 (2016).
7. S. Chen, J. Duan, M. Jaroniec, S.-Z. Qiao, Nitrogen and oxygen dual-doped carbon hydrogel film as a substrate-free electrode for highly efficient oxygen evolution reaction. *Adv. Mater.* **26**, 2925–2930 (2014).
8. P. Rasiyah, A. C. C. Tseung, The role of the lower metal oxide/higher metal oxide couple in oxygen evolution reactions. *J. Electrochem. Soc.* **131**, 803–808 (1984).
9. R. Subbaraman, D. Tripkovic, K.-C. Chang, D. Strmcnik, A. P. Paulikas, P. Hirunsit, M. Chan, J. Greeley, V. Stamenkovic, N. M. Markovic, Trends in activity for the water electrolyser reactions on 3*d* M(Ni,Co,Fe,Mn) hydr(oxy)oxide catalysts. *Nat. Mater.* **11**, 550–557 (2012).
10. A. Bergmann, E. Martinez-Moreno, D. Teschner, P. Chernev, M. Gliech, J. F. de Araujo, T. Reier, H. Dau, P. Strasser, Reversible amorphization and the catalytically active state of crystalline Co_3O_4 during oxygen evolution. *Nat. Commun.* **6**, 8625 (2015).
11. S. Yagi, I. Yamada, H. Tsukasaki, A. Seno, M. Murakami, H. Fujii, H. Chen, N. Umezawa, H. Abe, N. Nishiyama, S. Mori, Covalency-reinforced oxygen evolution reaction catalyst. *Nat. Commun.* **6**, 8249 (2015).
12. Z. Lu, G. Chen, Y. Li, H. Wang, J. Xie, L. Liao, C. Liu, Y. Liu, T. Wu, Y. Li, A. C. Luntz, M. Bajdich, Y. Cui, Identifying the active surfaces of electrochemically tuned $LiCoO_2$ for oxygen evolution reaction. *J. Am. Chem. Soc.* **139**, 6270–6276 (2017).
13. H. B. Tao, L. Fang, J. Chen, H. B. Yang, J. Gao, J. Miao, S. Chen, B. Lin, Identification of surface reactivity descriptor for transition metal oxides in oxygen evolution reaction. *J. Am. Chem. Soc.* **138**, 9978–9985 (2016).
14. B. Weng, F. Xu, C. Wang, W. Meng, C. R. Grice, Y. Yan, A layered $Na_{1-x}Ni_yFe_{1-y}O_2$ double oxide oxygen evolution reaction electrocatalyst for highly efficient water-splitting. *Energ. Environ. Sci.* **10**, 121–128 (2017).
15. Z. Xiao, Y. Wang, Y.-C. Huang, Z. Wei, C.-L. Dong, J. Ma, S. Shen, Y. Li, S. Wang, Filling the oxygen vacancies in Co_3O_4 with phosphorus: An ultra-efficient electrocatalyst for overall water splitting. *Energ. Environ. Sci.* **10**, 2563–2569 (2017).
16. B. Zhao, L. Zhang, D. Zhen, S. Yoo, Y. Ding, D. Chen, Y. Chen, Q. Zhang, B. Doyle, X. Xiong, M. Liu, A tailored double perovskite nanofiber catalyst enables ultrafast oxygen evolution. *Nat. Commun.* **8**, 14586 (2017).
17. I. Yamada, H. Fujii, A. Takamatsu, H. Ikeno, K. Wada, H. Tsukasaki, S. Kawaguchi, S. Mori, S. Yagi, Bifunctional oxygen reaction catalysis of quadruple manganese perovskites. *Adv. Mater.* **29**, 1603004 (2017).
18. J. Suntivich, K. J. May, H. A. Gasteiger, J. B. Goodenough, Y. Shao-Horn, A perovskite oxide optimized for oxygen evolution catalysis from molecular orbital principles. *Science* **334**, 1383–1385 (2011).
19. H. Xia, J. Dai, Y. Xu, Y. Yin, X. Wang, Z. Liu, M. Liu, M. A. McGuire, X. Li, Z. Li, C. Jin, Y. Yang, J. Zhou, Y. Long, Magnetism and the spin state in cubic perovskite $CaCoO_3$ synthesized under high pressure. *Phys. Rev. Mater.* **1**, 024406 (2017).
20. L. Youwen, K. Yoshio, I. Shintaro, T. Yasujiro, T. Yoshinori, Synthesis of cubic $SrCoO_3$ single crystal and its anisotropic magnetic and transport properties. *J. Phys. Condens. Matter* **23**, 245601 (2011).
21. A. Grimaud, O. Diaz-Morales, B. Han, W. T. Hong, Y.-L. Lee, L. Giordano, K. A. Stoerzinger, M. T. M. Koper, Y. Shao-Horn, Activating lattice oxygen redox reactions in metal oxides to catalyse oxygen evolution. *Nat. Chem.* **9**, 457–465 (2017).
22. M. W. Haverkort, Z. Hu, J. C. Cezar, T. Burnus, H. Hartmann, M. Reuther, C. Zobel, T. Lorenz, A. Tanaka, N. B. Brookes, H. H. Hsieh, H.-J. Lin, C. T. Chen, L. H. Tjeng, Spin state transition in $LaCoO_3$ studied using soft X-ray absorption spectroscopy and magnetic circular dichroism. *Phys. Rev. Lett.* **97**, 176405 (2006).

Acknowledgments

Funding: This work was supported by the Department of Energy, Office of Energy Efficiency and Renewable Energy (EERE) under award no. DE-EE000762 and Robert A. Welch Foundation of (Houston, TX) grant F-1066. X.L. also acknowledged the Beijing Institute of Technology Research Fund Program for Young Scholars. Y.Lo. was supported by the National Key R&D Program of China (grant 2018YFA0305700). **Author contributions:** J.B.G. supervised the project. Y.Li conceived the idea and designed the research. X.L., J.Z., Y.Lo., and C.J. prepared the sample and characterized the physical properties. H.W., Y.Li, Z.C., and S.X. did the other characterization and analyzed the data. Y.Li and J.B.G. wrote the paper. **Competing interests:** The authors declare that they have no competing interests. **Data and materials availability:** All data needed to evaluate the conclusions in the paper are present in the paper and/or the Supplementary Materials. Additional data related to this paper may be requested from the authors.

Submitted 4 October 2018
Accepted 27 June 2019
Published 9 August 2019
10.1126/sciadv.aav6262

Citation: X. Li, H. Wang, Z. Cui, Y. Li, S. Xin, J. Zhou, Y. Long, C. Jin, J. B. Goodenough, Exceptional oxygen evolution reactivities on $CaCoO_3$ and $SrCoO_3$. *Sci. Adv.* **5**, eaav6262 (2019).